Electron and hole gas in modulation-doped GaAs/$Al_{1-x}Ga_xAs$ radial heterojunctions

Andrea Bertoni* and Miquel Royo
CNR-NANO S3, Istituto Nanoscienze, Via Campi 213/a, 41125 Modena, Italy

Farah Mahawish and Guido Goldoni†
Department of Physics, University of Modena and Reggio Emilia and CNR-NANO S3, Istituto Nanoscienze, Via Campi 213/a, 41125 Modena, Italy

(Received 30 August 2011; revised manuscript received 3 November 2011; published 18 November 2011)

We perform self-consistent Schrödinger-Poisson calculations with exchange and correlation corrections to determine the electron and hole gas in a *radial* heterojunction formed in a GaAs/AlGaAs core-multi-shell nanowire, which is either *n*- or *p*-doped. We show that the electron and hole gases can be tuned to different localizations and symmetries inside the core as a function of the doping density/gate potential. Contrary to planar heterojunctions, conduction electrons do not form a uniform 2D electron gas (2DEG) localized at the GaAs/AlGaAs interface, but rather show a transition between an isotropic, cylindrical distribution deep in the GaAs core (low doping) and a set of six tunnel-coupled quasi-1D channels at the edges of the interface (high doping). Holes, on the other hand, are much more localized at the GaAs/AlGaAs interface. At low doping, they present an additional localization pattern with six separated 2DEGs strips. The field generated by a back-gate may easily deform the electron or hole gas, breaking the sixfold symmetry. Single 2DEGs at one interface or multiple quasi-1D channels are shown to form as a function of voltage intensity, polarity, and carrier type.

DOI: 10.1103/PhysRevB.84.205323 PACS number(s): 73.21.Hb, 73.21.Fg, 03.65.Ge

I. INTRODUCTION

Semiconductor nanowires (NWs) are rapidly evolving into functional nanomaterials,[1,2] strongly motivated by applications in energy harvesting[7–9] and electro-optical devices.[10] One key direction is the demonstration of core-multi-shell NWs (CSNWs), multilayered materials where free-standing NWs, grown *vertically* on top of a semiconductor surface, are used as a substrate for the *radial* overgrowth of multilayers.[3–6] The resulting system is a radial heterostructure (as in Fig. 1), grown radially and wrapped around the core. CSNWs brings together the self-assembling, bottom-up, quasi-1D nature of NWs and the flexible engineering of planar 2D heterostructures (which opened up decades of astonishing developments in fundamental physics and innovative applications). CSNWs have the potential to bring the field of NW-based devices to the level of a new key nanotechnology.

Critical steps have been taken in this direction. Long single-crystal, defect-free, untapered GaAs NWs, the material class of choice for quantum transport and high mobility, have been recently grown.[11,12] Epitaxial GaAs/AlGaAs multilayered structures can be realized with high-quality interfaces,[13] and selective *radial* doping has been demonstrated.[10] Self-catalytic or catalyst-free growth protocols have been developed, thus avoiding the use of Au, a source of deep trap formation.[5] High-mobility and ballistic transport, similar to GaAs planar structures, are therefore realistic targets in CSNWs in the short run.

A typical geometry, as the one investigated in this paper, is shown in Fig. 1. A GaAs NWs, which typically grows as hexagonal crystals along the [111] direction exposing the six {110} facets, is used as the core of the multilayer structure, which consists of an epitaxial AlGaAs shell, possibly including a doping layer, and a GaAs capping layer. Surface states easily deplete the outer layers, and a 2D electron or hole gas may localize at the inner GaAs/AlGaAs heterointerface. The latter consists of six planar *facets*, several tens of nm wide, interrupted by six *edges*. The confined electronic system has the sixfold symmetry of the NW used as a substrate.

It should be noted that in a typical heterojunction the electron gas extends into the GaAs layer by tens of nm, due to the balance between kinetic and Coulomb energy contributions. This is comparable to typical NWs diameters, and the electron gas on opposite sides of the GaAs core may strongly couple, as, e.g., in a double heterojunction.[14]

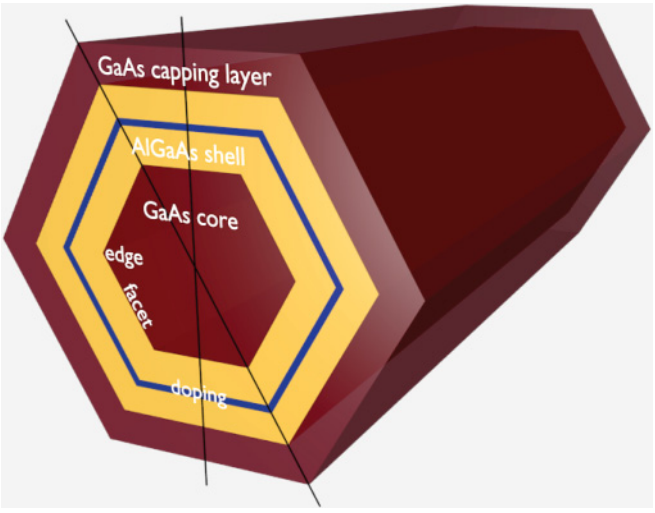

FIG. 1. (Color online) Schematics of a modulation-doped radial heterojunction in CSNW system. A GaAs core NW is covered by a AlGaAs shell, which is either *n*- or *p*-doped in the middle and capped by an additional GaAs layer. Eventually, an electron or hole gas forms in the core at the heterointerface with the AlGaAs shell. The two thin lines highlight the facet-to-facet and edge-to-edge directions, which will be specifically discussed in Sec. III [see also Eq. (9) and text below].

Therefore, the free electron gas formation in a CSNW is a genuinely two-dimensional problem (we assume the CSNW to be translationally invariant in one dimension). For example, it is easy to infer that for large doping or size of the structure, Coulomb energy will induce charge to localize along six quasi-1D channels at the edges of the interface, to maximize the average electron-electron distance.

Ab initio atomistic methods are computationally intensive and therefore limited to very thin NWs, 1–2 nm in diameter. Nonetheless, they can provide important informations on the band-alignment and dopant properties.[15–17] Modeling of larger CSNWs is also limited. Recently, the single-particle properties of a *cylindrical* electron gas have been simulated including strong homogeneous and inhomogeneous magnetic fields[18] and $k \cdot p$ effects.[19] Due to the prismatic geometry of CSNWs, cylindrical symmetry is broken, and localization at the edges of the heterointerface may take place.[20,21] Therefore, in NWs with diameters in the tens of nm range, the electronic system deviates substantially from the idealized cylindrical shape, and the electron gas may behave as a set of quasi-1D systems, rather than a uniform electron gas wrapped around the core. However, the above simulations neglect electron-electron interactions, and the confinement at the GaAs/AlGaAs interface is assumed, as in a narrow radial quantum well. As mentioned above, in doped structure the in-plane directions cannot be disentangled and full calculations need to be performed where the confinement is self-consistently included.[22]

In this paper, we discuss the formation of the electron and hole gas in GaAs/AlGaAs core-shell NWs, which are either n- or p-doped in the AlGaAs barriers. We will show that remote charge density, which forms at the inner GaAs/AlGaAs interface, may be tuned with doping and/or external gates changing the symmetry and localization of the distribution. The electron or hole gas has a mixed dimensionality, which is locally 1D or 2D. From this point of view, remarkable differences are found between electron and hole gases. We finally show that the electron or hole gas can be easily reshaped and tuned between 2D and 1D channels, which can be individually depleted by a transverse electric field applied by a back-gate, as in a field-effect-transistor (FET).

This paper is organized as follows. In Sec. II, the physical and numerical modeling is sketched, and the self-consistent procedure is described. In Sec. III, the results of our calculations are illustrated. First, we introduce the prototypical structure that we investigate and the relevant simulative parameters. Then, in subsections III B and III C, we report our results for n- and p-doped systems, respectively. The origin of the localization patterns is discussed in subsection III D, while subsection III E deals with a CSNW in FET device. Finally, in Sec. IV we draw our conclusions.

II. METHOD

The free electron or hole gas of a modulation-doped CSNW is obtained within an envelope-function approach in a single-band approximation, including carrier-carrier interaction at a mean-field level. The coupled system of Schrödinger and Poisson equations is solved by the usual self-consistent approach. Assuming translational invariance along the NW growth axis z, one obtains a 2D problem in the x,y plane. At each iteration of the self-consitent cycle, the effective-mass Schrödinger equations for electrons and holes,

$$\left\{-\frac{\hbar^2}{2}\nabla_{\mathbf{r}}\left[\frac{1}{m_e(\mathbf{r})}\nabla_{\mathbf{r}}\right] + E_c(\mathbf{r}) - eV(\mathbf{r})\right\}\phi_n^e(\mathbf{r}) = \epsilon_n^e\phi_n^e(\mathbf{r}), \tag{1}$$

$$\left\{-\frac{\hbar^2}{2}\nabla_{\mathbf{r}}\left[\frac{1}{m_h(\mathbf{r})}\nabla_{\mathbf{r}}\right] - E_v(\mathbf{r}) + eV(\mathbf{r})\right\}\phi_n^h(\mathbf{r}) = -\epsilon_n^h\phi_n^h(\mathbf{r}), \tag{2}$$

are solved on a 2D hexagonal domain representing the cross-section of the CSNW. Here, $\mathbf{r} = (x,y)$ is the 2D coordinate. m_e (m_h) is the material-dependent effective masse of electrons (holes), which is assumed isotropic in the x,y plane, and $E_c(\mathbf{r})$, $E_v(\mathbf{r})$, and $V(\mathbf{r})$ are, respectively, the local conduction-band edge, the valence-band edge, and the electrostatic potential generated by free carriers and fully-ionized dopants. The above equations are numerically integrated to give the set of eigenfunctions (eigenenergies) for electrons and holes $\phi^e(\mathbf{r})$ (ϵ^e) and $\phi^h(\mathbf{r})$ (ϵ^h), respectively.

After the solution of Eqs. (1) and (2) have been determined, the *volumetric* total charge density,

$$\rho(\mathbf{r}) = e[n_h(\mathbf{r}) - n_e(\mathbf{r}) + \rho_D(\mathbf{r}) - \rho_A(\mathbf{r})], \tag{3}$$

is calculated. Here, ρ_D and ρ_A are the ionized donor and acceptor densities, respectively. The densities of free electrons and holes are

$$n_e(\mathbf{r}) = 2\sum_n \left|\phi_n^e(\mathbf{r})\right|^2 \sqrt{\frac{\overline{m}_e(\mathbf{r})k_BT}{2\pi\hbar^2}}\mathcal{F}_{-\frac{1}{2}}\left(\frac{-\epsilon_n^e+\mu}{k_BT}\right), \tag{4}$$

$$n_h(\mathbf{r}) = 2\sum_n \left|\phi_n^h(\mathbf{r})\right|^2 \sqrt{\frac{\overline{m}_h(\mathbf{r})k_BT}{2\pi\hbar^2}}\mathcal{F}_{-\frac{1}{2}}\left(\frac{\epsilon_n^h-\mu}{k_BT}\right). \tag{5}$$

Here, $\overline{m}_e$ ($\overline{m}_h$) is the effective electron (hole) mass along the CSNW axial direction, which is in general different from the in-plane mass of Eqs. (1) and (2). T is the temperature, μ is the Fermi level, and $\mathcal{F}_k(x) = \frac{1}{\Gamma(k+1)}\int_0^\infty \frac{t^k dt}{e^{t-x}+1}$ is the complete Fermi-Dirac integral of order k, which results from the integration of the parabolic dispersion along the growth direction z.

The electrostatic potential V is computed from the total charge density by solving the Poisson equation with a material-dependent relative dielectric constant ε_r

$$\nabla_{\mathbf{r}}\left[\varepsilon_r(\mathbf{r})\nabla_{\mathbf{r}}V(\mathbf{r})\right] = -\frac{\rho(\mathbf{r})}{\varepsilon_0}. \tag{6}$$

Dirichlet boundary conditions are used, with the potential on the domain boundaries fixed to either an input value representing the voltage of a metallic gate in that position or zero. Several test simulations, with increasing domain size, confirm that the electrostatic potential at the CSNW surface is essentially zero when no gate is included.

The contribution due to exchange-correlation (XC) effects is calculated, via a local density approximation from the densities $n_e(\mathbf{r})$ and $n_h(\mathbf{r})$, and added to V, adopting the well-known approximate expression reported in Refs. 23 and 24. In all the simulations presented in the following, XC effects

turn out to be almost negligible.[22] For the sake of brevity, here we consider the XC contribution already included in V.

The procedure is iterated, with the new potential V inserted in Eqs. (1) and (2). The self-consistent cycle is stopped when the relative variation of the charge density is lower than a given value E_ρ at any position, i.e.,

$$\frac{A_{\max}|\rho(\mathbf{r}) - \rho'(\mathbf{r})|}{\int_A \rho(\mathbf{r})d\mathbf{r}} < E_\rho, \tag{7}$$

is fulfilled, where A is the area of the simulation domain.

Once convergence is achieved, the linear charge density of the NW can be calculated (we recall that the system is assumed to be translationally invariant along z) by the area integration

$$\rho_{\text{linear}} = \int_A \rho(\mathbf{r})d\mathbf{r}. \tag{8}$$

To compare the charge density at the heterointerface with a planar system, we also define the *effective* sheet charge density,

$$\rho_{\text{sheet}} = \frac{1}{2}\int_L \rho[\mathbf{r}(l)]dl, \tag{9}$$

where L is one of the two directions shown in Fig. 1, which either joins two edges or two facets, and $\mathbf{r}(l)$ is a point on one of these lines. ρ_{sheet} represents the sheet charge of an equivalent *planar* heterojunction, with a uniform charge along the interface. In our case, ρ_{sheet} is in general different in the two directions, and is an indication of the preferential localization of the free charge.

With regards to the numerical approach, the solutions of Schrödinger and Poisson equations are obtained through a box integration method[25] on a symmetry compliant triangular grid with hexagonal elements. This choice reproduces the shape of the domain and the symmetry of the (unbiased) system, and avoids numerical artifacts originated by discretization asymmetries of the six domain boundaries, as would be the case, e.g, using a rectangular grid. Formally, the partial differential equations Eqs. (1), (2), and (6) are integrated on each hexagonal element. By applying the divergence theorem, the area integral is converted in a linear integral of the flux along the hexagon boundary. A balance between incoming and outgoing fluxes (obtained through a first-order finite-differences scheme) of adjacent hexagons connects the unknowns on different elements. This results in a symmetric (Hermitian) sparse matrix for the Poisson (Schrödinger) equation, whose dimension corresponds to the number of hexagons, and with six nonzero elements on each row. The matrix for the Schrödinger equation is diagonalized through a Lanczos library algorithm[26] while that for the Poisson equation is solved, with the known term obtained from ρ, via an efficient library routine.[27] The Fermi-Dirac integral is computed by using an efficient routine implementing Chebyshev polynomial expansion.[28]

Stability of the self-consistent cycle for large and/or heavily doped structures is delicate. A standard mixing procedure using an under-relaxation parameter, α, is implemented. At iteration i, the electrostatic potential at the current iteration V^i is substituted by

$$V^i \leftarrow \alpha V^i + (1-\alpha)V^{i-1}. \tag{10}$$

TABLE I. Material parameters used in the simulations. ΔE_c and ΔE_v are the conduction and valence band offsets at the GaAs/$Al_{0.3}Ga_{0.7}As$ interface.[30] E_c and E_v are the conduction band and valence band edges, respectively. m_e and $\overline{m}_e$ are the relative electron effective masses in the x,y plane (orthogonal to the CSNW axis) and along the axis direction, z, respectively. Analogously, m_h and $\overline{m}_h$ are the hole masses. Note that the electron effective mass is assumed isotropic, while hole effective mass is strongly anisotropic.

	GaAs		$Al_{0.3}Ga_{0.7}As$
$E_c - E_v$ [eV]	1.43		1.858
ΔE_c [eV]		0.284	
ΔE_v [eV]		0.144	
m_e	0.067		0.092
$\overline{m}_e$	0.067		0.092
m_h	0.690		0.731
$\overline{m}_h$	0.105		0.124
ε_r	13.18		12.24

Although the Poisson and Schrödinger equations are solved on the same discrete lattice, the charge density extends very little into the AlGaAs barriers, due to the large depletion operated by surface states. Typically, we require the wave functions to vanish at the position of the doping layer. Therefore, the Schrödinger equation needs to be solved only in a subset of points of the entire lattice.

Holes are treated in a single-band approach, too. As we shall discuss in subsection III C, the hole gas is mostly confined at the GaAs/AlGaAs interfaces, which are directed along the six {110} directions. The parabolic dispersion for heterostructures grown along the [110] direction is given in Ref. 29 [Eq. (4.4a)]. The strongly anisotropic mass is heavy in the [110] direction (roughly twice the mass along the widely used [100] direction) and light along in-plane direction, here corresponding to the vertical growth direction [111], as shown later in Table I.

III. RESULTS

A. Structure and simulation details

As a prototype structure (see Fig. 1), we simulate a device similar to the one described in Ref. 6. A GaAs core 80 nm wide is surrounded by a 50-nm-wide $Al_{0.3}Ga_{0.7}As$ shell and by a 10-nm-wide GaAs capping layer. The $Al_{0.3}Ga_{0.7}As$ shell is uniformly doped in the center with a 10-nm-wide layer at a constant doping density ρ_D of donors and ρ_A of acceptors. Material parameters are shown in Table I. μ is taken at the mid-gap value of GaAs, and all calculations are performed at $T = 20$ K.

In this section we report results for n- and p-doped structures. In both cases, the occupation probability of minority carriers is negligible. Hence, we need to solve only the relevant equation, among Eqs. (1) and (2). Schrödinger and Poisson equations are solved on a 2D hexagonal domain, discretized with a regular hexagonal tessellation. Our simulations typically use about 2×10^5 hexagonal elements. The Schrödinger equation is solved on a subset of 5×10^4 elements, as explained in the previous section. The under-relaxation parameter $\alpha = 0.05$ and the maximum convergence relative error allowed in the charge density $E_\rho = 10^{-3}$. Convergence is typically achieved within 100–200 iterations

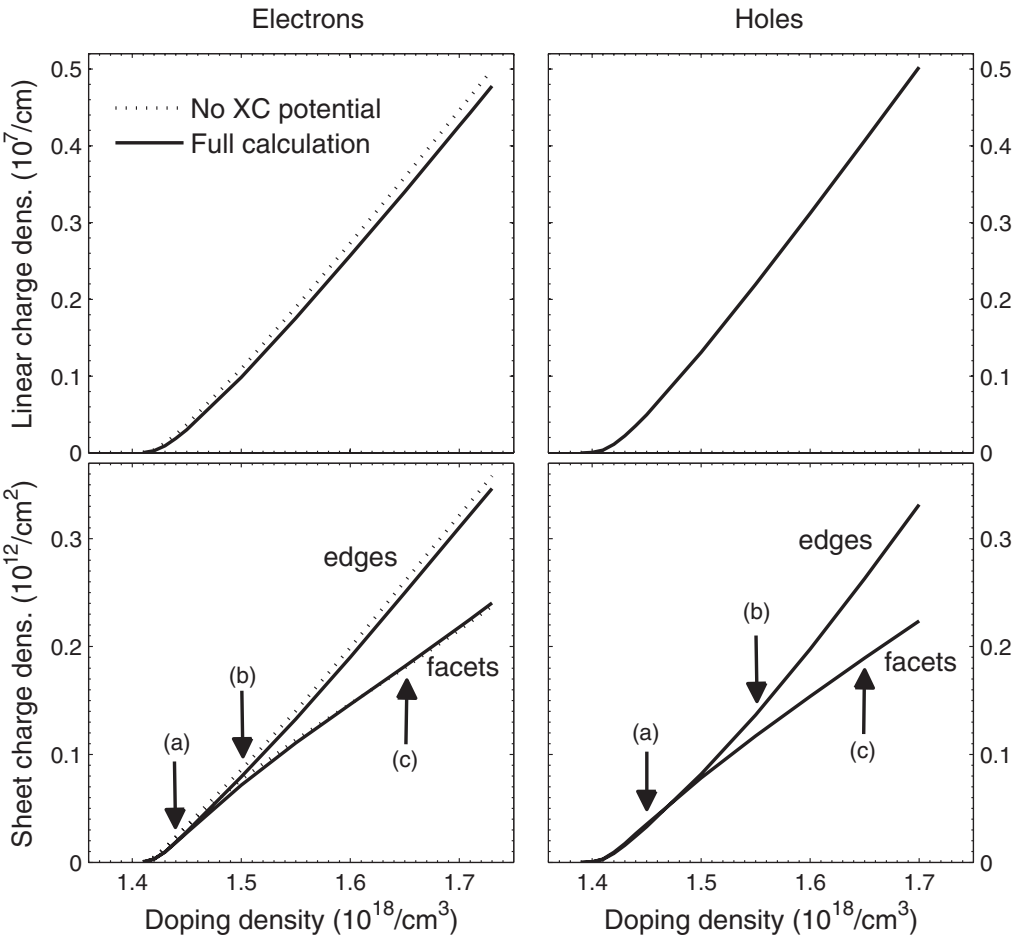

FIG. 2. Top: Linear charge density of the free-electron gas (right) and free-hole gas (left) as a function of the donor density ρ_D. Bottom: sheet charge density of the free-electron gas (right) and free-hole gas (left) calculated along the facet-to-facet and edge-to-edge directions indicated in Fig. 1. Arrows indicate three different densities shown in Fig. 3 for electrons, and Fig. 5 for holes. As the doping density increases, the free carriers tend to accumulate on the six CSNW edges and form six 1D channels. In the graphs for electrons, results of self-consistent calculations neglecting XC contributions are also reported (dotted curve).

if the potential V at the first iteration is zeroed. The number of iterations is substantially reduced by initializing the potential with a suitable guess, as, e.g., the converged potential at a slightly different doping density. Of course, converged results do not depend on this choice.

B. Electron gas localization

We now consider an n-doped CSNW, where a free-electron gas is eventually formed in the GaAs core or at the inner heterointerface. Specifically, we investigate the free electron gas formation as a function of the doping density ρ_D. Figure 2 (top-left panel) shows the linear free-electron density vs. ρ_D. At a threshold density $\sim 1.4 \times 10^{18}$ cm^{-3} the NW starts to be populated, in qualitative agreement with Refs. 10 and 6. The linear density is a fraction of $\sim 10^7$ cm^{-1} and increases linearly with doping. Note the tiny difference between the calculations with and without the XC potential. All the results reported in the rest of the paper include the XC potential.

The charge density maps reported in Fig. 3 show that the free-electron gas is localized in the GaAs core, as expected. Indeed, at sufficiently large doping, the conduction band bends down from the surface value until the Fermi level (zero in the right energy scale of the right plots of Fig. 3), which is pinned to the middle of the gap at the CSNW surface. This is in complete analogy to the formation of an inversion layer in a remotely doped planar heterojunction. However, here the localization is not homogeneous along the heterointerface, and its pattern strongly depends on the doping density, as we discuss next.

In Fig. 2 (bottom-left panel) we show the sheet charge density given by Eq. (9) on facets and on edges. At small doping the two densities are equal, while at larger doping the edge population becomes dominant. This evolution is made more clear in the charge density maps of Fig. 3, which refer to the three densities labeled (a), (b), and (c) in Fig. 2, namely 1.44, 1.5, and 1.65×10^{18} cm^{-3}. At the lowest doping, shown in Fig. 3(a), the GaAs core starts to be populated, and the charge is distributed deep into the core. The distribution is only slightly modulated (right panels) crossing the core along either the facet-to-facet or edge-to-edge directions, and slightly depleted in the center of the core. Furthermore, the distribution is almost circularly symmetric. Accordingly, the two sheet charge densities in Fig. 2 are equal.

As the doping is increased [Fig. 3(b)] the charge depletion in the center is more pronounced, and the charge moves toward the interfaces. The 2D map (left panel) shows that

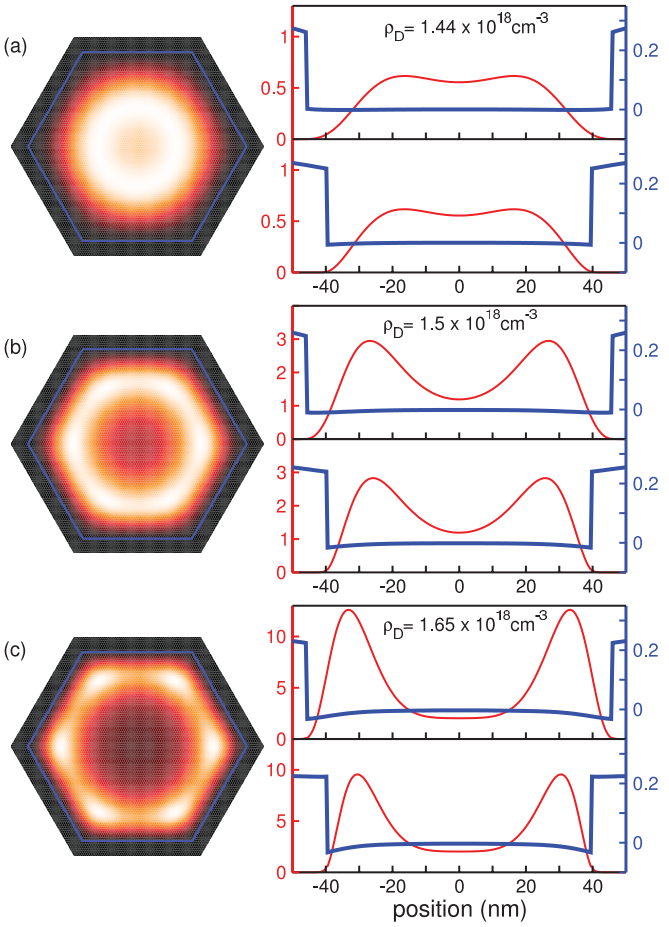

FIG. 3. (Color online) Spatial distribution of the free-electron gas for the three values of the doping density ρ_D indicated as (a), (b), and (c) in Fig. 2 (bottom-left panel). ρ_D values are reported on the right graphs. For each density we show (left) the 2D map of the charge, with the GaAs/AlGaAs interface indicated as a solid line, and (right) the charge density profile (thin line, left axis, units of 10^{16} cm^{-3}) and the self-consistent conduction-band profile (thick line, right axis, units of eV, $\mu = 0$) along the edge-to-edge direction (right, top) and along the facet-to-facet direction (right, bottom). Note the different scales for different doping densities.

the distribution is starting to develop a sixfold symmetry, and the sheet charge density along the edge-to-edge direction is starting to dominate. For large doping [Fig. 3(c)], the charge is strongly localized at the edges. This can be seen in the 2D map (left panel) as well as, more quantitatively, in the two profiles (right panels). In this regime the charge density has fully developed the sixfold symmetry and resembles a set of coupled quantum wires more than a 2DEG: most of the charge is confined in relatively narrow channels at the edges, while only a minor part of the charge sits at the facets.

The charge density is obtained from the occupation of an increasing number of energy subbands. The evolution of subband energies against the doping density is shown in Fig. 4 with respect to the Fermi energy. As the doping increases, subbands fall more and more below the Fermi level. Due to the sixfold symmetry, these states are singly or doubly degenerate, as indicated.

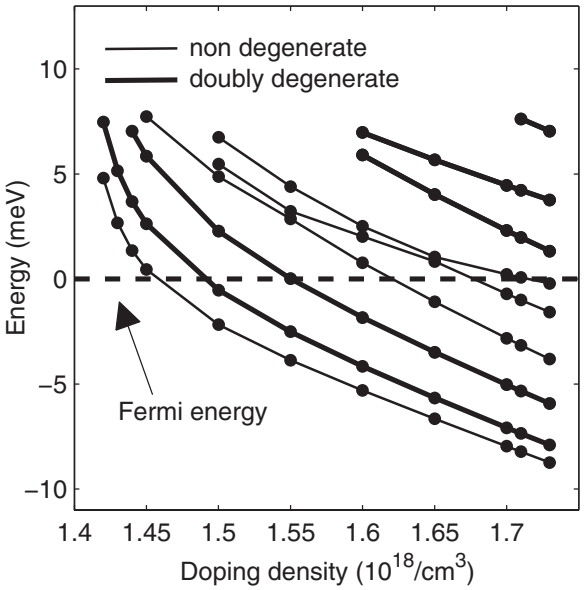

FIG. 4. Electron subband energy vs. doping density ρ_D. Each bullet represents the subband edge resulting from the self-consistent calculation. The lines (thinner for nondegenerate subbands, thicker for doubly degenerate subbands) are a guide to the eyes.

C. Valence band holes

Nanowires are easily p-doped. For example, Si is amphoteric for GaAs.[31] In this section, we discuss the formation of the hole gas in the same structure of the previous section. We use a parabolic band approximation with the appropriate effective masses, as discussed in Sec. II and reported in Table I. Due to the parabolic approximation, the difference between electron and hole gases to be discussed below reside only in the much heavier effective mass of holes.

Figure 2 shows the free-charge density of holes as a function of the doping level. Similar to the electron gas, there is a threshold doping density, $\sim 1.4 \times 10^{18}$ cm^{-3}, below which no free charge is obtained. Above this threshold, the linear charge density (top-right panel) increases linearly, as for conduction electrons. The equivalent sheet charge density (bottom-right panel of Fig. 2) along the edge-to-edge and facet-to-facet directions of the structure also behaves similar to the case of electrons. In particular, at low doping the two densities are similar, with the sheet charge density at the edges taking over when the doping increases.

However, it turns out that holes have a very different localization pattern with respect to conduction electrons, in particular at low and intermediate doping. Figure 5 shows the free-hole density profiles at the three densities (a), (b), and (c) indicated in Fig. 2 (bottom-right panel), namely 1.45, 1.55, and 1.65 $\times 10^{18}$ cm^{-3}. Although the sheet charge density is nearly equal in the two directions at the lowest density, the hole density is peaked at the facets, while the distribution along the edge-to-edge direction is low at the edges and broader toward the core. This is in sharp contrast to conduction electrons, where at low doping the charge forms a cylindrical distribution in the core.

At intermediate densities [Fig. 5(b)], the gap between the facets is filled, and the hole gas is uniformly distributed at

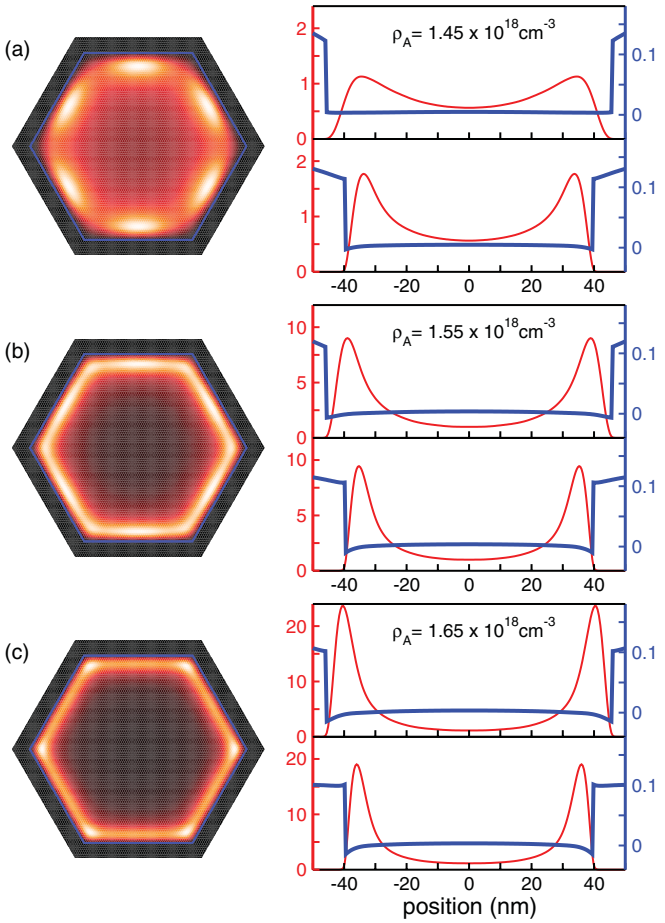

FIG. 5. (Color online) Spatial distribution of the free-hole gas for the three values of the doping density ρ_A, indicated as (a), (b), and (c) in Fig. 2 (bottom-right panel). ρ_A values are reported on the right graphs. For each density we show (left) the 2D map of the charge, with the GaAs/AlGaAs interface indicated as a solid line, and (right) the charge density profile (thin line, left axis, units of 10^{16} cm^{-3}) and the self-consistent valence-band profile (thick line, right axis, units of eV, $\mu = 0$) along the edge-to-edge direction (right, top) and along the facet-to-facet direction (right, bottom). At the lowest doping (a), the free holes are localized mainly along the facets, contrary to the electron case. At intermediate doping (b), the free holes form an hexagonal ring, a regime which has no counterpart for conduction electrons.

the GaAs/AlGaAs interfaces. Only weak modulations are present along the interface going around the core in this very interesting intermediate regime. Therefore, in this case the hole gas indeed resembles a 2D hole gas, which is sixfold bent around the wire. This regime has no counterpart for conduction electrons. Finally, at the largest density [Fig. 5(c)], instead, the charge is concentrated at the edges.

The evolution of the hole subbands with doping density ρ_A, not shown here, is similar to that of conduction electrons, except for a larger density of levels due to the heavier mass. Typical energy splittings are a small fraction of an meV.

D. Origin of localization patterns

To rationalize the behavior of electrons and holes vs. doping, in particular at low density, we can consider the following three energy contributions. (1) Repulsive Coulomb energy between like particles, which requires maximization of the average interparticle distance and therefore favors localization at the edges of the inner GaAs/AlGaAs interface. (2) *Vertical* localization energy, which is the kinetic energy required to localize charge at the GaAs/AlGaAs interfaces, similar to a planar heterojunction. (3) *Lateral* localization energy, which is the energy required to localize parallel to the interface, along a facet or at an edge, the latter being clearly larger.

At low density, when the Coulomb contribution is small, conduction electrons distribute over the core, since vertical localization energy is large. Lateral localization would be also dominant over the small Coulomb energy in this regime. Hence, the isotropic cylindrical symmetry. The charge gets localized near the GaAs/AlGaAs interfaces only if the density and the average Coulomb energy is so large that localization at the edges is energetically favorable. Indeed, in this regime the small additional cost in lateral localization energy at the edges with respect to facets is overcompensated by gain in Coulomb energy due to interedge repulsion. However, for holes, the small kinetic energy (one order of magnitude smaller than for conduction electrons) makes it easier to localize at the accumulation layer near the interface, even at very low densities. Since the Coulomb energy is always small in this

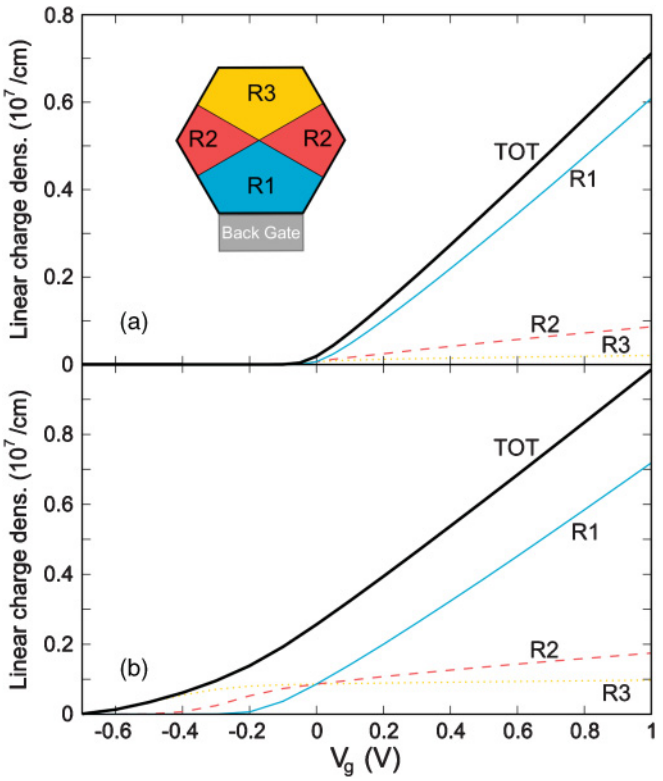

FIG. 6. (Color online) Linear electron density integrated over the three domains of the NW illustrated in the inset, as a function of the gate voltage. Solid blue lines are used for the domain labeled as R1, dashed red lines for R2, and dotted yellow lines for R3. The total electron density is also plotted in thick solid black lines. Two densities of n-dopants are represented: (a) 1.4×10^{18} cm^{-3} and (b) 1.64×10^{18} cm^{-3}.

regime, hole density may localize at the facets rather than at the edges, where the lateral confinement energy would be larger.

We finally note that the localization depends essentially on the amount of free charge, which in the present calculation is tuned by the doping density. Alternatively, one could fix the doping density to a large value and deplete the electron (hole) gas by using an external gate around the wire. The different localization regimes shown above can be obtained using a proper voltage applied to it. We have explicitly calculated the charge evolution by simulating an all-around gate and indeed recovered results (not shown) very similar to the doping-modulated structures. In the next section, we will show instead what happens by application of a back-gate to a NW.

E. Biased system

Transport properties of NWs can be measured by integrating them in planar FETs.[32,33] In such devices, a NW is placed on a substrate covered by a dielectric layer, which separates the wire from another layer acting as a global back gate. The applied gate voltage depletes or populates the NWs depending on its sign. Thus, it can be used to modulate the conductance between the source and drain electrodes. We next simulate the effect of such a back gate, assuming that it is in remote contact with one of the external facets of the NW, hereafter referred to as the bottom facet (see inset in Fig. 6). The potential is set to $V = -eV_g$ on the basis edge, where V_g is the applied electrode voltage in the range $V_g = \pm 1$ V. Since the boundary of our simulation domain corresponds to the CSNW surface and it is at least 60 nm distant from the free carriers, we assume that the possible modulations of V along the edges have little influence on the carrier localization in the core.

In Fig. 7 we show the electron charge density profiles at four selected gate voltages for two NWs with a low (left) and high (right) density of dopants. As anticipated, the charge density no longer shows the symmetric distributions obtained at zero voltage and tends to accumulate at the top and bottom of the wire section for negative and positive voltages, respectively. Interestingly, for the NW with higher density of dopants we observe how the six quasi-1D channels obtained at zero voltage can be switched to four and two channels by tuning the voltage

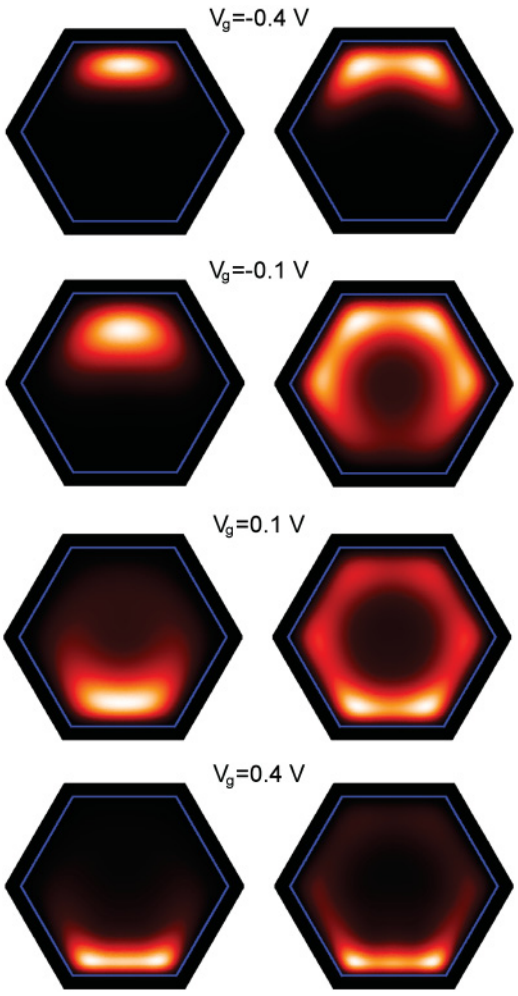

FIG. 7. (Color online) Spatial distribution of the free-electron gas in two CSNWs with doping densities $1.4 \times 10^{18}\,\mathrm{cm}^{-3}$ (left) and $1.64 \times 10^{18}\,\mathrm{cm}^{-3}$ (right) at four selected values of the gate voltage. Depending on the sign of the voltage, the free electrons tend to localize near the top or bottom parts of the wire.

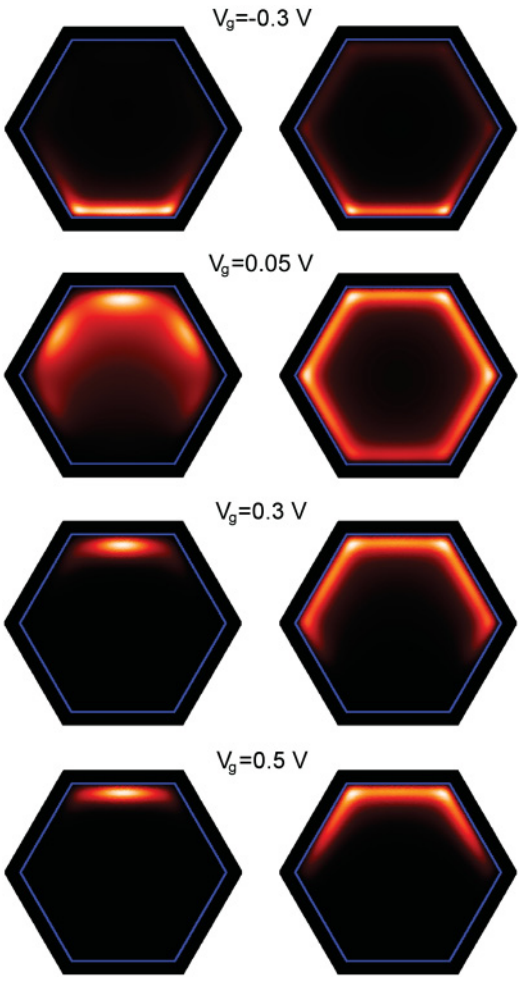

FIG. 8. (Color online) Spatial distribution of the free-hole gas in two CSNWs with doping densities $1.45 \times 10^{18}\,\mathrm{cm}^{-3}$ (left) and $1.65 \times 10^{18}\,\mathrm{cm}^{-3}$ (right) at four selected values of the gate voltage. New charge arrangements are observed not present in the electron-gas case, e.g., the charge accumulation at the three top facets of the wire ($V_g = 0.05$ V).

to $V_g = -0.1$ V and $V_g = \pm 0.4$ V. Also, note the different localization for negative voltages at low or high doping, where charge is distributed in a broad channel or in two narrower channels, respectively.

The quantitative effect of the gate voltage can be observed in Fig. 6, where we represent the linear charge density obtained by integrating the volume charge density over the three domains depicted in the inset, as a function of the applied voltage. The total linear charge density is also plotted (black solid line). Clearly, the three curves coincide at zero bias due to symmetry. A positive gate voltage does not deplete the top regions of the wire in favor of a larger electronic concentration in the bottom of the wire. Instead, the charge density raises quasilinearly in all regions. This increase is much pronounced in the bottom regions R1 and R2, while in region R3 the charge remains nearly constant at the zero bias value. On the other hand, the evolution of the charge density is not linear when the NW becomes depleted by applying negative voltages. This fact can be associated with the smaller density of subbands to populate at such low-density regimes. Finally, we notice that at high positive voltages both systems reach the same density regime with the electrons concentrated at the two bottom edges of the wire (see, e.g., bottom plots in Fig 7), despite the different density of dopants.

Figures 8 and 9 show the corresponding results for hole populated NWs with two different densities of dopants, lower

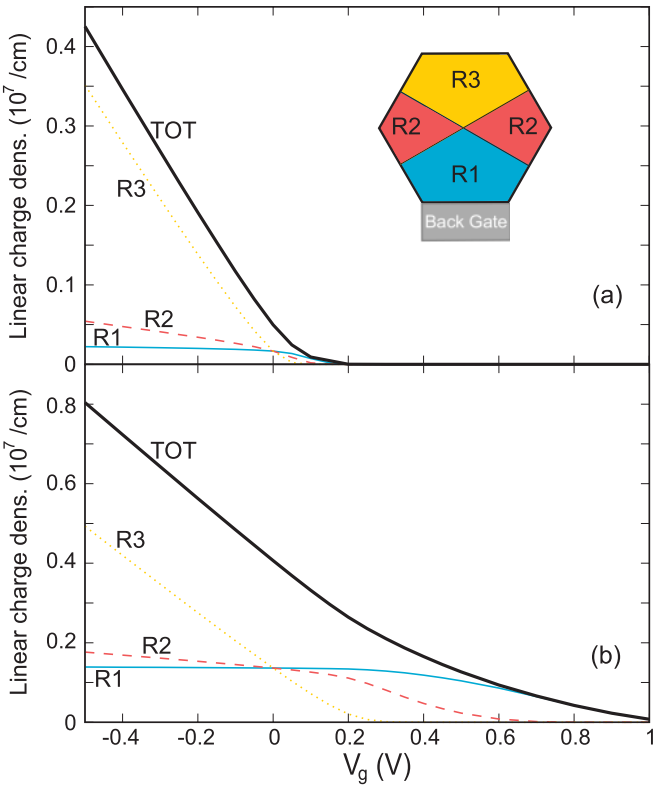

FIG. 9. (Color online) Linear hole density integrated over the three domains of the NW illustrated in the inset, as a function of the gate voltage. Solid blue lines are used for the domain labeled as R1, dashed red lines for R2, and dotted yellow lines for R3. The total hole density is also plotted in thick solid black lines. Two densities of p-dopants are represented: (a) 1.45×10^{18} cm^{-3} and (b) 1.65×10^{18} cm^{-3}.

on the left, higher on the right. Clearly, the applied voltage induces the opposite effect than in the electronic system, increasing (decreasing) and localizing the charge density at the bottom (top) of the NW at negative (positive) voltages. In parallel with the result obtained at zero voltage, the NW with higher density of p-dopants shows qualitatively the same behavior as its n-doped counterpart. Thus, in the right panels of Fig. 8, it can be seen that a NW with two and four quasi-1D hole channels can be attained by properly tuning the applied voltage. Nevertheless, the trend of the hole density to localize in the facets at low-density regimes enables the observation of new voltage-induced charge arrangements when the density of dopants is lower. For instance, at $V_g = 0.05$ V the charge density is concentrated in the center of the three top facets, while at $V_g = -0.3$ V a 2D hole gas is clearly formed over the bottom facet.

To conclude, in Fig. 9 we show the effect of the gate voltage on the linear hole density integrated over the three regions of the NW. The results are equivalent to the electronic case, with the role of the three regions reversed due to the opposite sign of the carriers, and can be rationalized along the same lines.

IV. CONCLUSIONS

We have determined the properties of an electron and hole gas in a realistic model of *radial* heterojunctions formed in a modulation-doped GaAs/AlGaAs CSNW. Different localization and symmetry regimes can be realized as a function of the doping level and/or by a back-gate. Contrary to planar heterojunctions, conduction electrons do not form a 2DEG well localized at the GaAs/AlGaAs interface but rather show transitions between different charge distributions across the section of the CSNWs. For conduction electrons, these are similar to phases predicted in GaN/AlGaN CSNWs.[22] Specifically, we find (i) a cylindrical charge distribution deep in the GaAs core, and (ii) a set of six tunnel-coupled quasi-1D channels at the edges of the interface, at low doping and high doping levels, respectively. For p-doped structures, the heavier effective mass results in additional phases for the hole gas, which have no counterpart for conduction electrons. In particular, with increasing doping levels it is possible to form (i) six separated planar 2DEGs at the GaAs/AlGaAs interfaces, (ii) a quasi-uniform sixfold bent 2DEG, (iii) six tunnel-coupled quasi-1D channels at the edges.

In general, however, our results show that the electron and hole gases in these structures deviate substantially from an isotropic distribution at the GaAs/AlGaAs heterointerfaces. Depending on the doping density and, possibly, the applied gate potential, the charge density reshapes between quasi-1D and quasi-2D distributions and moves between facets and edges localization. This might also have an impact on the effectiveness of different scattering mechanisms in different regimes.

ACKNOWLEDGMENTS

We acknowledge useful discussions with S. Roddaro, H. Shtrikman, A. Kretinin, I. Zardo, D. Spirkoska, and R. Calarco. We acknowledge partial financial support from MIUR-FIRB RBIN06JB4C and MIUR-PRIN 2008H9ZAZR.

*andrea.bertoni@nano.cnr.it
†guido.goldoni@unimore.it

[1] C. M. Lieber, MRS Bull. **28**, 486 (2003).
[2] C. M. Lieber and Z. L. Wang, MRS Bull. **32**, 99 (2007).
[3] A. Fontcuberta i Morral, D. Spirkoska, J. Arbiol, M. Heigoldt, J. R. Morante, and G. Abstreiter, Small **4**, 899 (2008).
[4] M. Keplinger, T. Martensson, J. Stangl, E. Wintersberger, B. Mandl, D. Kriegner, V. Holý, G. Bauer, K. Deppert, and L. Samuelson, Nano Lett. **9**, 1877 (2009).
[5] M. Heigoldt, J. Arbiol, D. Spirkoska, J. M. Rebled, S. Conesa-Boj, G. Abstreiter, F. Peiro, J. R. Morante, and A. Fontcuberta i Morral, J. Mater. Chem. **19**, 840 (2009).
[6] K. Sladek, V. Klinger, J. Wensorra, M. Akabori, H. Hardtdegen, and D. Grützmacher, J. Cryst. Growth **312**, 635 (2010).
[7] X. Z. B. Tian, T. J. Kempa, Y. Fang, N. Yu, G. Yu, J. Huang, and C. M. Lieber, Nature (London) **449**, 885 (2007).
[8] C. Colombo, D. Spirkoska, M. Frimmer, G. Abstreiter, and A. Fontcuberta i Morral, Phys. Rev. B **77**, 155326 (2008).
[9] J. A. Czaban, D. A. Thompson, and R. R. LaPierre, Nano Lett. **9**, 148 (2009).
[10] K. Tomioka, J. Motohisa, S. Hara, K. Hiruma, and T. Fukui, Nano Lett. **10**, 1639 (2010).
[11] H. Shtrikman, R. Popovitz-Biro, A. Kretinin, and M. Heiblum, Nano Lett. **9**, 215 (2009).
[12] H. Shtrikman, R. Popovitz-Biro, A. Kretinin, L. Houben, M. Heiblum, M. Bukała, M. Galicka, R. Buczko, and P. Kacman, Nano Lett. **9**, 1506 (2009).
[13] M. J. Tambe, S. K. Lim, M. J. Smith, L. F. Allard, and S. Gradečak, App. Phys. Lett. **93**, 151917 (2008).
[14] K. Inoue, H. Sakaki, J. Yoshino, and T. Hotta, J. Appl. Phys. **58**, 4277 (1985).
[15] Y. Zhang, L.-W. Wang, and A. Mascarenhas, Nano Lett. **7**, 1264 (2007).
[16] M. Amato, S. Ossicini, and R. Rurali, Nano Lett. **11**, 594 (2011).
[17] M. Rosini and R. Magri, ACS Nano **4**, 6021 (2010).
[18] G. Ferrari, A. Bertoni, G. Goldoni, and E. Molinari, Phys. Rev. B **78**, 115326 (2008).
[19] V. V. Ravi Kishore, B. Partoens, and F. M. Peeters, Phys. Rev. B **82**, 235425 (2010).
[20] G. Ferrari, G. Goldoni, A. Bertoni, G. Cuoghi, and E. Molinari, Nano Lett. **9**, 1631 (2009).
[21] Y. Masumoto, K. Goto, S. Yoshida, Y. Sakuma, P. Mohan, J. Motohisa, and T. Fukui, Phys. Rev. B **82**, 075313 (2010).
[22] B. M. Wong, F. Leonard, Q. Li, and G. T. Wang, Nano Lett. **11**, 3074 (2011).
[23] O. Gunnarsson and B. I. Lundqvist, Phys. Rev. B **13**, 4274 (1976).
[24] T. Ando, H. Taniyama, N. Ohtani, M. Nakayama, and M. Hosoda, J. Appl. Phys. **94**, 4489 (2003).
[25] S. Selberherr, *Analysis and Simulation of Semiconductor Devices* (Springer, New York, 1984).
[26] R. B. Lehoucq, C. Sorensen, and D. C. Yang, *ARPACK Users Guide: Solution of Large-Scale Eigenvalue Problems with Implicitly Restarted Arnoldi Methods* (SIAM, Philadelphia, 1998).
[27] O. Schenk, M. Bollhoefer, and R. Roemer, SIAM Rev. **50**, 91 (2008).
[28] A. J. MacLeod, ACM Trans. Math. Software **24**, 1 (1998).
[29] G. Fishman, Phys. Rev. B **52**, 11132 (1995).
[30] C. Bosio, J. L. Staehli, M. Guzzi, G. Burri, and R. A. Logan, Phys. Rev. B **38**, 3263 (1988).
[31] J. Dufouleur, C. Colomb, T. Garma, B. Ketterer, E. Uccelli, M. Nicotra, and A. F. i Morral, Nano Lett. **10**, 1734 (2010).
[32] M. Mescher, B. Marcelis, L. de Smet, E. Sudholter, and J. Klootwijk, IEEE Trans. Electron Devices **58**, 1886 (2011).
[33] J. Tang, C.-Y. Wang, F. Xiu, M. Lang, L.-W. Chu, C.-J. Tsai, Y.-L. Chueh, L.-J. Chen, and K. L. Wang, ACS Nano **5**, 6008 (2011).